"Dissecting" Landscapes with Hölder Exponents to reconcile process and form

C. J. Keylock[1], A. Singh[2], P. Passalacqua[3], and E. Foufoula-Georgiou[4]

[1]School of Architecture, Building and Civil Engineering, Loughborough University, Loughborough, Leicestershire, LE11 3TU, UK.
[2]Department of Civil, Environmental and Construction Engineering, University of Central Florida, 12800 Pegasus Drive, Orlando, FL 32816-2450, USA
[3]Department of Civil, Architectural and Environmental Engineering, Cockrell School of Engineering, The University of Texas at Austin, 301 E. Dean Keeton St., C1700, Austin, TX 78712-0273, USA
[4]Henry Samueli School of Engineering, Engineering Hall 5400 (EH 5400), University of California Irvine, CA 92697-2175, USA

Key Points:

- Terrain statistics are compared to null models that preserve multi-Hölder or multi-fractal structure
- Various geomorphometric measures show landscape is more complex than multi-fractal models suggest
- Diffusive processes act to increase landscape complexity after a flux equilibrium is established.

Corresponding author: Chris Keylock, c.j.keylock@lboro.ac.uk

Abstract

A long-standing question in geomorphology concerns the applicability of statistical models for elevation data based on fractal or multifractal representations of terrain. One difficulty with addressing this question has been the challenge of ascribing statistical significance to metrics adopted to measure landscape properties. In this paper, we use a recently developed surrogate data algorithm to generate synthetic surfaces with identical elevation values as the source dataset, while also preserving the value of the Hölder exponent at any point (the underpinning characteristic of a multifractal surface). Our primary data are from an experimental study of landscape evolution. This allows us to examine how the statistical properties of the surfaces evolve through time and the extent to which they depart from the simple (multi)fractal formalisms. We also study elevation data from Florida and Washington State. We are able to show that the properties of the experimental and actual terrains depart from the simple statistical models. Of particular note is that the number of sub-basins of a given channel order (for orders sufficiently small relative to the basin order) exhibit a clear increase in complexity after a flux steady-state is established in the experimental study. The actual number of basins is much lower than occur in the surrogates. The imprint of diffusive processes on elevation statistics means that, at the very least, a stochastic model for terrain based on a local formalism needs to consider the joint behavior of the elevations and their scaling (as measured by the pointwise Hölder exponents).

1 Introduction

A landscape is an assemblage of individual, identifiable features that can be classified and explained by the geomorphologist [*Arrell et al.*, 2007; *Ehsani and Quiel*, 2008; *Passalacqua et al.*, 2010; *Clubb et al.*, 2014], and also the parts in between that are a palimpsest of current and past processes [*Jerolmack and Paola*, 2010]. A focus on individual landscape features can be key to unlocking the geological history of a region [*Gasparini et al.*, 2014], while consideration of the landscape as a whole using measures such as the hypsometric integral [*Strahler*, 1952; *Boon III and Byrne*, 1981; *Brocklehurst and Whipple*, 2004; *Keylock et al.*, 2020b], or statistical scaling laws topography [*Hack*, 1957; *Tokunaga*, 1978; *Willgoose*, 1994; *Lague and Davy*, 2003; *Zanardo et al.*, 2013] gives an insight in to how uplift, erosion and deposition interact to shape our landscapes. From the perspective of this latter approach, the question remains as to the extent that statistical models for topography can adequately represent observed elevation statistics. Expressed another way, do the particular dynamics of geomorphic processes leave an imprint on the terrain that makes simple statistical models inadequate?Addressing this question forms the goal of this paper.

The complex configuration and environmental history of a landscape make a formal, mathematical or statistical description of terrain regularity problematic. Attempts to do this have commonly adopted methods based on the notion of fractal dimension [*Klinkenberg and Goodchild*, 1992; *Lifton and Chase*, 1992; *Outcalt and Melton*, 1992; *Gagnon et al.*, 2006]. However, the generalization of the description of landscape from monofractal to one where more than a single fractal dimension is present has resulted in significant terminological confusion. In order to try to resolve this, we propose the definitions given in Table 1. Our table incorporates two commonly adopted descriptions of the statistical scaling of terrain elevations: fractal (here, monofractal) [*Klinkenberg and Goodchild*, 1992] and multifractal [*Lavallée et al.*, 1993; *Gagnon et al.*, 2006]. Unifying both these descriptions is the principle that a description of elevation statistics may be accomplished in terms of pointwise Hölder regularity [Jaffard, 1997]. This is by far the most common form of regularity used to describe time-series or surface data, although other possibilities exist [*Arnéodo et al.*, 1998; *Seuret and Lévy Véhel*, 2003]. Monofractality assumes that the Hölder exponent describing the terrain is constant everywhere (it is a Hurst exponent), while multifractality is used in a general sense to mean that the Hölder exponent varies. Here, we use the term “multi-Hölder” rather than “multifractal” for this general no-

Table 1. Terminology used in this paper concerning the regularity classes and descriptions of topography

Name	Description
Monofractal surface	A surface described effectively by a Hurst exponent. There is no significant difference in the Hölder exponent in space. A fractional Brownian surface with constant Hölder exponent [*Mandelbrot and van Ness*, 1968].
Multi-Hölder surface	A surface described by multiple Hölder exponents.
Multi-fractional Brownian Surface	A multi-Hölder surface where the variability in Hölder exponent is given by a continuous function as seen with multi-fractional Brownian motion [*Peltier and Lévy Véhel*, 1995].
Multifractal surface	A multi-Hölder surface where the Hölder exponents are imbricated, leading to either a non-continuous or a random description of their variation.
Conditional multi-Hölder surface	A multi-Hölder surface of either type where the variation in the Hölder exponent exhibits significant association with another variable.
Self-regulating multi-Hölder surface	A special case of a conditional multi-Hölder surface, where the conditioning variable is the elevation. Hence, the statistics of the elevation derivatives are not independent of the elevations [*Lévy Véhel*, 2013].

tion of a terrain where the Hölder exponents vary. This allows us to contrast a "multifractal" surface with a "multi-fractional Brownian surface" in terms of how the variability is structured. A multifractal surface is one that is the outcome of a hierarchical process such that individual Hölder exponents are imbricated in a non-continuous fashion [*Benzi et al.*, 1993], while a multi-fractional Brownian surface is one where the variability is given by a continuous function [*Peltier and Lévy Véhel*, 1995]. Self-regulating processes are relatively recent development in regularity theory where the regularity is coupled to the values of the signal [*Echelard et al.*, 2015]. This concept underpins the velocity-intermittency method for extracting information on flow structures from turbulence time series [*Keylock et al.*, 2012; *Ali et al.*, 2019; *Keylock et al.*, 2020a]. In addition to this idea of self-regulation, Table 1 also includes the more general category of a "conditional multi-Hölder surface", where the Hölder exponents are a function of some other terrain property, with the self-regulating process being a special case where this conditioning is on the elevation itself.

While previous work has shown that geomorphic surfaces are not monofractal [*Evans and McLean*, 1995; *Perron et al.*, 2008], the nature and extent to which a multi-Hölder description of landscape is appropriate is still unclear. While some authors have suggested that a multifractal model is suitable [*Gagnon et al.*, 2006], others have been more cautious. Of particular importance in this context is a study by *Veneziano and Iacobellis* [1999] that not only critiqued the methodologies adopted in some previous works, but also showed that for various terrains, there was evidence of consistent self-similar relations for both the channel network part of the terrain where fluvial incision was dominant, and the hillslopes dominated by diffusive processes. In other words, landscapes are a conditional multi-Hölder surface, dependent on a categorization into hillslope and channel network.

A difficulty with all previous investigations of this phenomenon is the absence of an appropriate control that may be used to compare extracted statistical quantities from topographic surfaces and determine their statistical significance. Given that some of these

phenomena are rather subtle in nature, as well as the error in any statistical curve-fitting exercise used for deriving a scaling relation, this is important. In this study, we develop a framework that permits analysis of landscape scaling properties relative to appropriate control models for the topography. We apply this framework to investigate the extent to which elevation statistics contain a signature from geomorphic processes that cannot be represented adequately by simple multi-Hölder models for terrain statistics. To accomplish this, we make use of a laboratory experiment on terrain evolution [*Singh et al.*, 2015], as well as digital elevation models (DEMs) from Florida and Washington State.

2 Experimental set-up

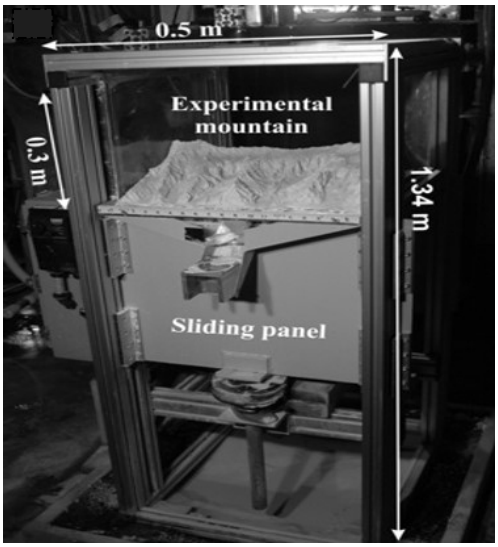

Figure 1. Illustration of the eXperimental Landscape Evolution (XLE) facility at the University of Minnesota.

Experiments were performed at the eXperimental Landscape Evolution (XLE) facility of the St. Anthony Falls Laboratory at the University of Minnesota (Fig. 1). XLE consisted of a 0.5 x 0.5 x 0.3 m^3 erosion box with two opposing sides able to slide up and down at variable rates mimicking changes in the base level. The facility includes a rainfall simulator consisting of 20 ultrafine misting nozzles which were able to generate rain droplets of sizes less than 10 μm. The experimental setup was also equipped with a laser scanner able to scan the experimental topography at resolution of 0.5 mm in a few seconds. This was done every 300 seconds for over nine hours. In this study we report results in time increments corresponding to this 300 s interval. Thus, $t = 30$ equates to 9,000 seconds. The experimental landscapes discussed here were evolved under constant uplift, $U = 20$ mm h^{-1}, and precipitation intensity, $P = 45$ mm h^{-1}. The erodible material was a homogeneous mixture of fine silica (specific density ~ 2.65) with a grain size distribution of $D_{25} = 10\mu$m, $D_{50} = 25\mu$m, and $D_{75} = 45\mu$m, mixed with 35% water by volume in a cement mixer; see *Singh et al.* [2015]; *Tejedor et al.* [2017] for more details. The key changes that arose in the evolution of the topography were the establishment of a drainage basin at $t \sim 30$ (150 minutes), the main drainage divide at $t \sim 45$ (225 minutes), a steady-state landscape in terms of sediment flux at $t \sim 75$ (375 minutes), and a final evolution towards a morphometric steady-state for $t \gtrsim 95$ (475 minutes).

3 Methodology

Previous work has had difficulty discriminating between the various descriptions of terrain provided in Table 1 because of the absence of a suitable testing framework that can permit differences between cases to be assessed with statistical confidence. Thus, to make progress in this field, a new methodology is required. Our formulation of this problem is based on the concept of surrogate data, which have been used for about thirty years for hypothesis testing for non-linear processes in time-series signal processing [*Theiler et al.*, 1992]. This field, including geophysical applications of the salient methods, was recently reviewed by *Keylock* [2019]. In brief, the most well-known approach is to employ an algorithm that preserves the Fourier amplitudes of a signal and the values of the signal itself, but randomizes the Fourier phases. This is known as the iterated, amplitude adjusted Fourier transform (IAAFT) method [*Schreiber and Schmitz*, 1996]. Given a linear version of the original signal (i.e. a realization of an autoregressive process), comparison of the original data to the surrogates allows various forms of non-linearity to be detected. In addition, one can determine if the variation in Hölder exponents is sufficient for a signal to be significantly different to monofractal and exhibit statistical intermittency [*Poggi et al.*, 2004; *Venema et al.*, 2006; *Basu et al.*, 2007; *Keylock*, 2009].

Given the rejection of such a hypothesis of linearity, gradual reconstruction [*Keylock*, 2010] can then be used to determine how complex a signal is. For example, *Keylock et al.* [2014b] used gradual reconstruction to show how the complexity of river bed topography was a function of discharge, with the superposition of intermediate scale bedforms driving this complexity. *Schwenk and Foufoula-Georgiou* [2017] used this approach to show that the planform of river meanders encodes information on process nonlinearities, with the behavior of pre-cutoff and post-cutoff meander bends contrasted. *Keylock et al.* [2015] applied this approach to a multi-Hölder model for turbulence and were able to show the statistical significance of relatively small coefficients in a Fokker-Planck model for the velocity increments.

Analysis using surrogate data generated with the IAAFT algorithm is highly suited to distinguishing between mono-fractal signals and any of the class of multi-Hölder signals described in Table 1. However, it cannot be used to discriminate between multi-Hölder surfaces, which is the focus of this study. An algorithm for this class of problem was presented by *Keylock* [2017] and developed in to a gradual reconstruction framework by *Keylock* [2018]. Before we describe this technique we briefly review the definition of pointwise Hölder regularity, as this underpins the characterization of the various multi-Hölder surfaces we defined in the introduction.

3.1 Hölder exponents

Given a DEM containing elevations, $z(x, y)$, the increments (the elevation differences between points at separation, r) are:

$$\delta z = z(x, y) - z(x + r\cos\theta, y + r\sin\theta), \tag{1}$$

where θ is a direction selected for analysis and r is the separation distance between points. The statistical moments of order n for δz are given by $\langle \delta z^n \rangle$, where the angled braces indicate an averaging operation. The scaling relation

$$\langle |\delta z|^n \rangle \propto r^{\xi_n}, \tag{2}$$

is then found from a log-log plot of $\langle |\delta z|^n \rangle$ against r. A fractal form for the distribution of elevations implies that ξ_n increases linearly with n [*Frisch and Parisi*, 1985]. In the well-known case of classical turbulence theory, the Kolmogorov [1941] theory gives $\xi_n = \frac{1}{3}n$.

A multi-Hölder signal exhibits a convex relation between n, and ξ_n [*Frisch and Parisi*, 1985], but is more formally concerned with the set of pointwise Hölder scaling ex-

ponents, S_h that characterize the properties of the surface. At a particular position, $z(x = X, y = Y)$ we can evaluate the local scaling behavior of z to determine the Hölder exponent, h, in a fashion that is similar to the statistical moments of the increments, above, but without the averaging operator:

$$|z(X,Y) - Z(X + r\cos\theta, Y + r\sin\theta)| \sim C|r|^{h(x,y)} \tag{3}$$

where C is a constant (see *Venugopal et al.* [2006] for a review). Having applied (3) to the whole DEM, the singularity spectrum, $D(h)$, is given by the set of values for h for which S_h is not empty. The Frisch-Parisi conjecture states that

$$D(h) = \min_n(hn - \xi_n + 1). \tag{4}$$

Thus, the structure functions and the Hölder exponents are related via a Legendre transform [Jaffard, 1997]. Therefore, a mono-fractal landscape has a constant degree of proportionality between n and ξ_n, giving a single constant value for $D(h)$: the Hurst exponent, d. The fractal dimension of the surface would then be $\mathscr{D} = 2 + (1 - d)$.

3.2 Hypothesis testing with surrogate data

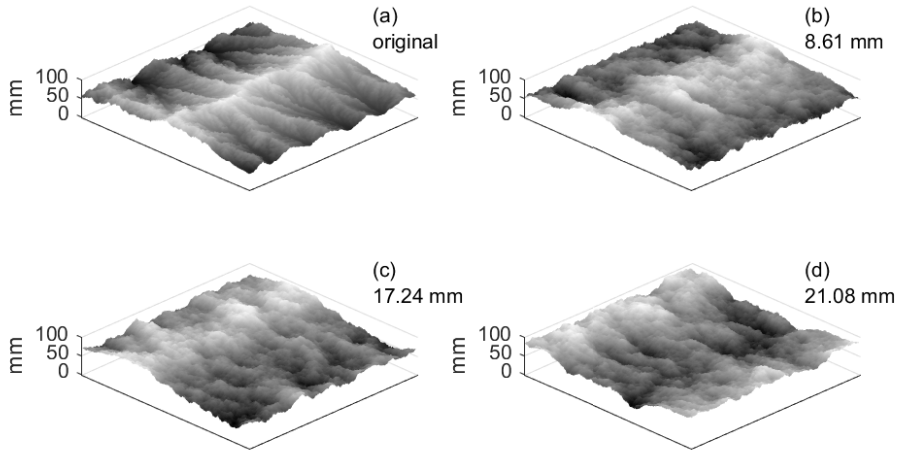

Figure 2. The original DEM at $t = 100$ is shown in (a), while (b), (c) and (d) show three surrogate DEMs for this surface generated with the IAAFT algorithm with the minimum, median and maximum root-mean-squared differences in the elevations, z, of 19 surrogates.

Figure 2 shows one DEM from our experiment [*Singh et al.*, 2015], together with three example surrogates generated by the Fourier amplitude-preserving IAAFT algorithm. The chosen three DEMs are those with the minimum, median and maximum root-mean-squared differences in elevation between the surrogate DEM and the original DEM at $t = 100$. Note that this does not imply one synthetic DEM is better than another; it just shows the degree of variation intrinsic to the randomization process. The strong visual constrast between the actual terrain and the surrogates implies straightaway that a mono-fractal description is inappropriate for describing this surface. This qualitative assessment may be formalized by generating a total of b surrogate datasets and, assuming a two-tailed statistical test, if the value for the original data on some measure are greater than or less than that for all b surrogates, the null hypothesis may be rejected at a significance level of $\alpha = 2/(b + 1)$, and this is what we do below.

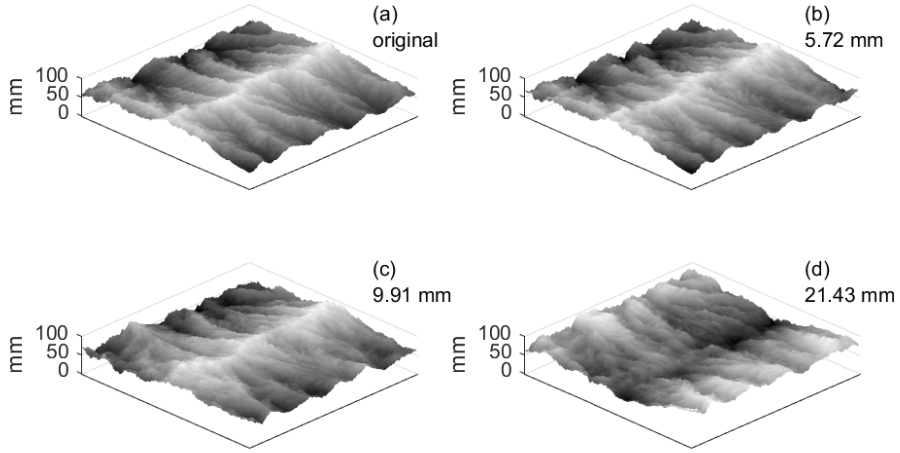

Figure 3. The original DEM at $t = 100$ is shown in (a), while (b), (c) and (d) show three surrogate DEMs for this surface generated with the IAAWT algorithm with the minimum, median and maximum root-mean-squared differences in the elevations, z, of 19 surrogates.

Rather than using the IAAFT method, in this study we generate surrogate surfaces with exactly the same elevation values as the original surface and the same Hölder regularity at a given point in the terrain using the iterated, amplitude adjusted wavelet transform (IAAWT), which was first presented by *Keylock* [2017]. A description of this algorithm and the associated gradual reconstruction methodology is provided in the Appendix. In brief, the IAAWT algorithm is conceptually similar to the IAAFT algorithm but replaces Fourier phase-randomization with a wavelet phase-randomization based on the dual-tree complex-valued wavelet transform [*Kingsbury*, 2001]. As a consequence, the algorithm produces surrogate data that fix in place the Hölder exponents for the original surface, as well as sampling the elevations from the same set of values as contained in the original DEM. Figure 3 is similar to Fig. 2 but uses the IAAWT as the surface-generating algorithm. Even though the terrain elevations are randomized (panel (d) has a valley where the original DEM has its main ridge), it is visually clear that this algorithm generates much more realistic topographies.

The differences between the IAAFT and IAAWT methods are formalized in Fig. 4. The left-most panels show the mean of the absolute part of the Fourier transform of all 512 horizontal and 512 vertical profiles extracted from the DEM as a function of frequency, ω in radians as a black line, together with the results for the surrogates for the IAAFT (a) and IAAWT (d) algorithms. A power-law fit is also shown as a dashed line, indicating that there is 'mono-fractal-like' behavior exhibited by these data. Because the IAAFT algorithm preserves the Fourier amplitudes, not surprisingly there is no visible difference between data and surrogates on this measure. The IAAWT algorithm also replicates the observed behavior of the Fourier amplitudes to a good level of accuracy but, in addition, it preserves the multi-Hölder properties as can be seen in the difference in the histograms for the pointwise Hölder exponents, h in (b) and (e). This is summarized more effectively by the boxplots in (c) and (f), where the former examines the mean value for h for data and surrogates, and the latter the standard deviation.

Gradual multifractal reconstruction (GMR) introduces a control parameter for the surrogate data generation, $0 \leq \eta \leq 1$, where $\eta = 0$ equates to surrogates generated by the IAAWT algorithm (full wavelet phase randomization) and $\eta = 1$ is the original data (no

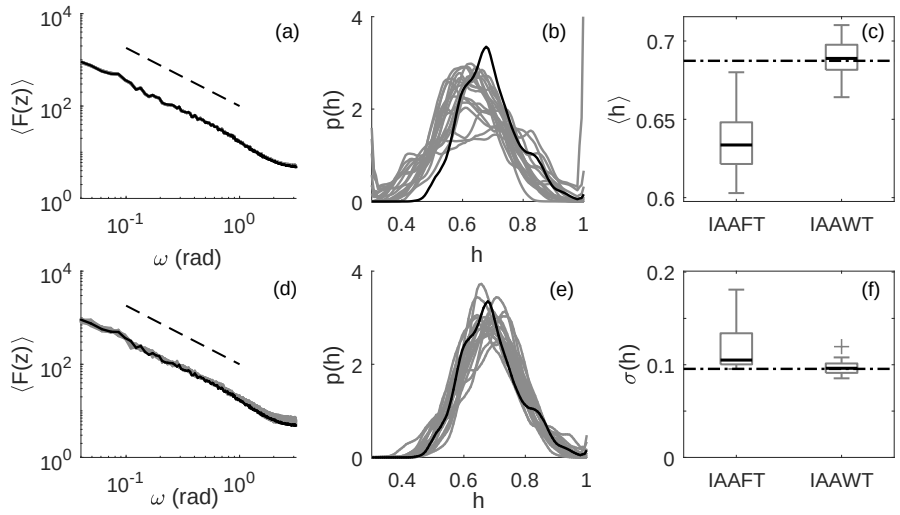

Figure 4. Statistical properties of the original DEM at $t = 100$ and the surrogate data. Panels (a) and (b) show results using the IAAFT algorithm and panels (d) and (e) are for the IAAWT algorithm. In each of these four panels, results for the original data are shown in black and for the surrogates in gray. Panels (a) and (d) illustrate the spectral properties of the DEMs with a best-fit power-law shown as a dashed line (displaced vertically). Panels (b) and (e) are the histograms of the pointwise Hölder exponents, h. Panels (c) and (f) show boxplots of the values of the mean and standard deviation for h, respectively, for nineteen surrogates DEMs generated with the IAAFT and IAAWT algorithms. The values from the original DEM are shown by a horizontal dot-dashed line. The box delimits the lower and upper quartiles with the central bar the median. Whiskers extend for up to 1.5 times the inter-quartile deviation, with outliers shown as crosses.

wavelet phase randomization) [*Keylock*, 2018]. Having selected a value for η, appropriate surrogates are generated by fixing in place a subset of the wavelet coefficients based on an energy criterion as described in the Appendix. With this framework it is then possible to define a threshold value for, η, denoted η^* above which there is no significant difference between data and surrogates. This can be used as a measure of the complexity of the topography [*Keylock et al.*, 2014b] and is employed in this study as a way of summarizing our results.

3.3 Geomorphometric measures

In this study, we draw upon three basic classes of geomorphometric analysis. The first is based on the slope-area relation, which *Willgoose* [1994] showed was highly relevant to the study of evolving topographies with both tectonic and climatological forcing. The second class utilizes the notion of Horton-Strahler channel ordering to classify subcatchments in the DEM into different basin orders, Ω. For all of the basins of a given order, we then derived the number of basins at that order, $N_B(\Omega)$, and the average total channel length for a given order, $\langle \sum L(\Omega) \rangle$. Typically, power-law relations for these quantities are found [*Rodgriguez-Iturbe and Rinaldo*, 1997]. However, here we focus on the raw values rather than the fitted exponent to contrast with the approach taken with slope-area scaling. These first and second class of geomorphometric measures are similar to those adopted in related work [*Singh et al.*, 2015; *Tejedor et al.*, 2017]. Our third method is a recently proposed variant of terrain hypsometry [*Strahler*, 1952], but modified to include simultaneous consideration of the Hölder regularity of a landscape [*Keylock et al.*, 2020b].

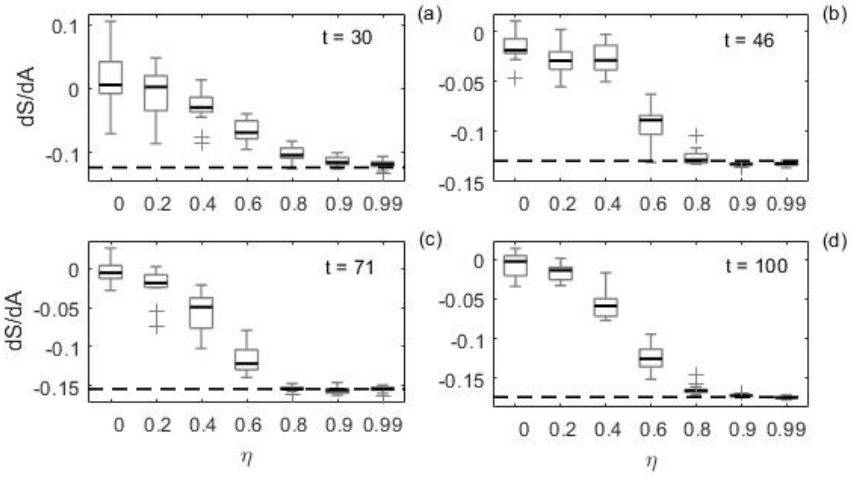

Figure 5. Boxplots showing values of dS/dA for the original DEM (horizontal, dashed line) and surrogates (boxplots) as a function of η. The threshold, η^* is obtained by working from right to left until the last case is found for which there is no signficant difference between data and surrogates. This gives $\eta^* = \{0.8, 0.6, 0.8, 0.9\}$ for $t = 30$, $t = 46$, $t = 71$, and $t = 100$, respectively. The boxplots are formulated in the same way as in Fig. 4.

For the analysis of the experiment we employed seven η values ($\eta \in \{0.0, 0.2, 0.4, 0.6, 0.8, 0.9, 0.99\}$) and generated 19 surrogate DEMs for each of twenty-two experimental DEMs using gradual multifractal reconstruction (i.e. 22 original and 2,926 synthetic DEMs were analyzed). These spanned the times from when the drainage basin was first established at $t \sim 30$, through the attainment of a flux equilibrium at $t \sim 70$, to beyond the development of a morphometric steady-state at $t \sim 95$.

4 Results

4.1 Slope-area relations

Figure 5 shows how the threshold values, η^* are determined for the slope-area scaling, dS/dA, for DEMs obtained at four instances that span the experimental duration. All DEMs clearly have values for dS/dA that depart from those obtained from a simple multi-Hölder representation of the terrain at $\eta = 0$. Once the central drainage divide is established in the experiment, i.e. for $t \gtrsim 30$, the surrogate landscapes differ from the actual DEM for $\eta \leq 0.4$. With 19 surrogates generated and a directional, one-tailed hypothesis that dS/dA for the surrogates is not significantly greater than for the original DEM, our analysis indicates a significant difference at the 5% level up to $\eta = 0.8$ for most cases.

Given values for $\eta^*(dS/dA)$ for all 22 DEMs, Fig. 6b shows how these vary as a function of the evolution of the catchment. All values are high and there is a possible weak tendency in these results with random variability in the range $0.6 < \eta^*(dS/dA) \leq 0.9$ up until a flux equilibrium is established at $t \sim 70$, followed by a gradual increase in $\eta^*(dS/dA)$ beyond this point. Figure 6a shows the values for dS/dA as a function of time, with a quadratic decay illustrated by a red line. The vertical lines extending from each symbol show a form of confidence interval that is possible using surrogate data analysis [*Keylock*, 2012]; one based on the range of values for the surrogates at the appropriate $\eta^*(t)$, rather than quality of fit to one set of data. It is clear that: (a) the one instance of $\eta^*(dS/dA) = 0.6$, at $t = 45$, is a consequence of a great range to the fitted slopes at this time; and, (b) the change in dS/dA with time is significant.

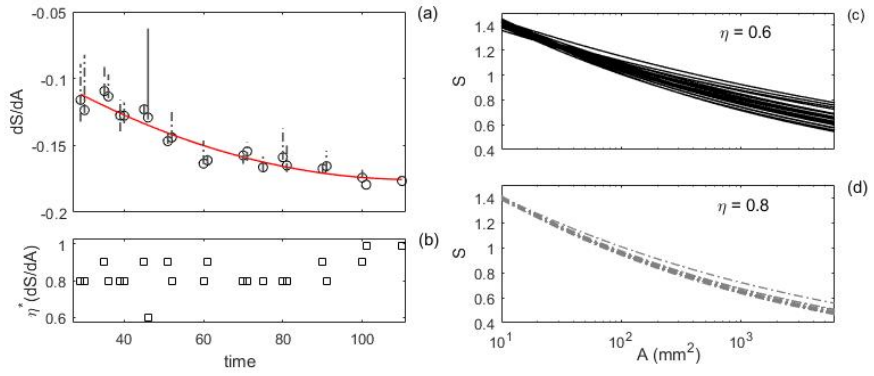

Figure 6. The slope-area scaling exponent as a function of the DEM number (time, t) is shown in panel (a) as a circle, with a best-fit quadratic as a red curve. The vertical dark gray lines show the range of values for the gradual multifractal reconstruction (GMR) surrogates at the value for $\eta^*(dS/dA)$, with $\eta^*(dS/dA) = 0.6$ (solid), $\eta^*(dS/dA) = 0.8$ (dash-dotted), and $\eta^*(dS/dA) = 0.9$ (dashed). The variation for $\eta^*(dS/dA) = 0.99$ is little greater than the size of the circles. Panel (b) shows these values for $\eta^*(dS/dA)$ as a function of time. Panels (c) and (d) show the relation between basin slope and upstream contributing area for the surrogate data at $t = 100$ for $\eta = 0.6$ (c) and $\eta = 0.8$ (d). Results are shown on semi-logarithmic axes for clarity, although all fits are of a power-law form.

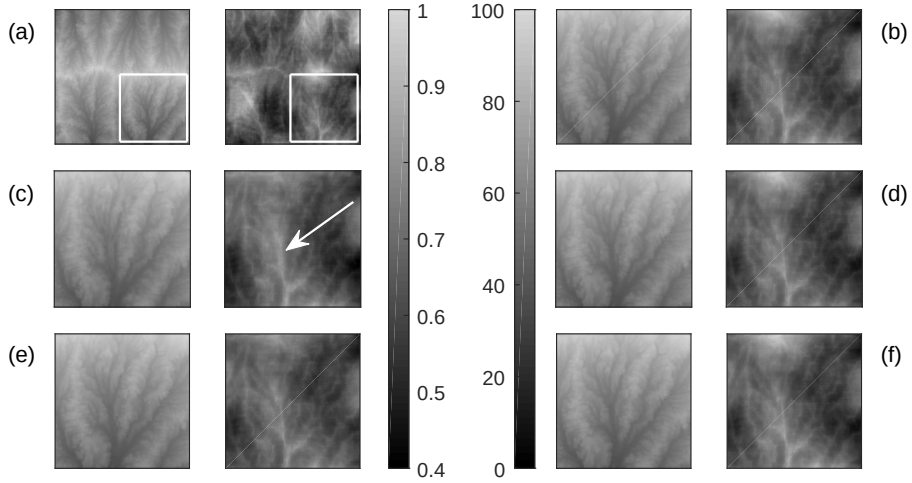

Figure 7. The DEM extracted at $t = 100$ in plan view, together with accompanying surrogate data. In each of six cases, two panels are shown with the left-hand cases illustrating the elevations, z, and the right-hand the Hölder exponents. Panel (a) is the original DEM with a white box showing the region extracted in the other panels. Panel (b) is this extracted region, (c) is the surrogate DEM at $\eta = 0.6$ with the median value for dS/dA, while (d), (e) and (f) are the surrogate DEMs at $\eta = 0.8$ with the median value, maximum and minimum values for dS/dA, respectively. The arrow highlights a feature discussed in the text.

In order to understand why the $\eta^*(dS/dA)$ values are generally high, in Fig. 6c and d we plot the fitted power-laws for the surrogates using the DEM for $t = 100$ as an exam-

ple. For $\eta = 0.6$ and $\eta = 0.8$ the slopes for the small area basins are the same (~ 1.4), while they are significantly lower for the large basins at $\eta = 0.8$. Hence, we can explain why the surrogates cannot replicate the dS/dA values at low η: the slopes of the larger basins are too steep. As small basins are typically located in the headwater catchments, the true landscape has a stronger coupling between lower elevations and reduced gradients, implying some degree of self-regulation as defined in Table 1, and as considered in section 5. Thus, the shortcomings of a simple multi-Hölder model are less in the representation of the dissected, upper basins but rather in the correct representation of the deposition-dominated, larger catchments.

To illustrate the difficulty of detecting these differences by observation and, thus, the difficulty of evaluating the verisimilitude of a multi-Hölder model by qualitative assessment, we show in Fig. 7 the detail of the original data and various surrogate DEMs for $t = 100$. Panel (a) shows a plan view of the original DEM, while panel (b) highlights the region in the white box in panel (a). From Fig. 5d, the surrogate DEM at $\eta = 0.6$ with the median value for dS/dA and that at $\eta = 0.8$ with the maximum for dS/dA shown in panels (c) and (e), respectively, are in error, while the surrogate at $\eta = 0.8$ with the median and minimum for dS/dA shown in (d) and (f), respectively, are very close to the original case. The highlighted area of the DEM is one containing a large basin consisting of low elevations and high values for h. The primary visible difference is that the spine of high h values in (c) indicated by the arrow is too broad and diffuse relative to the cases seen in panels (b), (d) and (f). This results in high h values being associated with somewhat higher z values than in the original DEM, causing reduced values for dS/dA at $\eta = 0.6$ compared to the true case. Clearly, a surrogate data framework is needed to extract such subtleties with statistical confidence.

4.2 Average total channel length

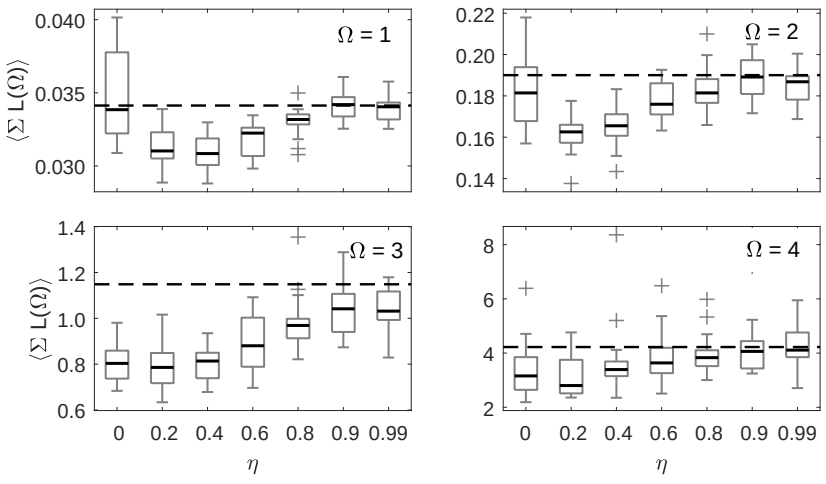

Figure 8. Boxplots showing the determination of $\eta^*(L)$ for the DEM at $t = 30$ for basin orders $\Omega \in \{1, 2, 3, 4\}$. The values of $\langle \sum L(\Omega) \rangle$ for the surrogates are shown as boxplots a function of η, with the dashed lines showing the value for the data itself. From these plots, $\eta^*(L) = \{0.8, 0.6, 0.8, 0.0\}$ for ascending values of Ω. The boxplots are formulated in the same way as in Fig. 4.

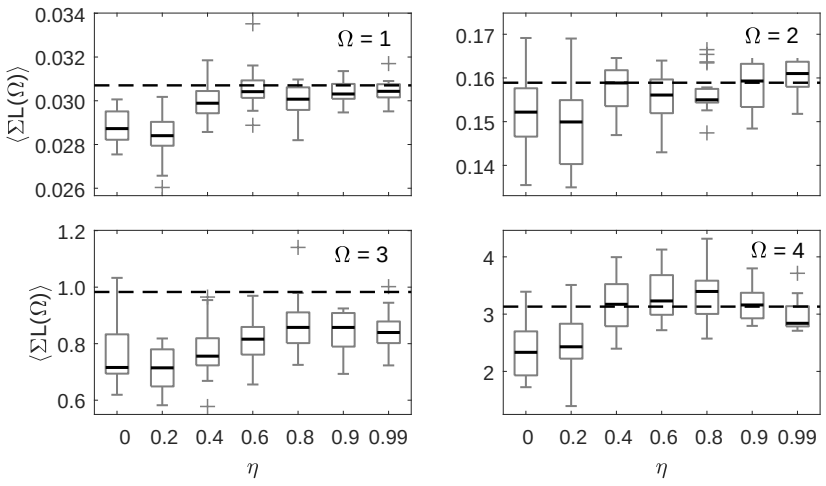

Figure 9. Boxplots showing the determination of $\eta^*(L)$ for the DEM at $t = 100$ for basin orders $\Omega \in \{1, 2, 3, 4\}$. The values of $\langle \sum L(\Omega) \rangle$ for the surrogates are shown as a function of η, with the dashed lines showing the value for the data itself. From these plots, $\eta^*(L) = \{0.4, 0.0, 0.99, 0.0\}$ for ascending values of Ω. The boxplots are formulated in the same way as in Fig. 4.

Figures 8 and 9 show the average channel length for basins of four Horton-Strahler orders at two different times as a function of η. These results contrast with the slope-area scaling as a simple multi-Hölder model with no additional constraints ($\eta = 0$) can replicate the observed channel lengths in many cases, even though η^* itself is often greater. Furthermore, in neither case do the fourth order basins indicate any significant differences. These are the largest in the system and are integrating information over a sufficiently large area that the preservation of the elevations and the approximate preservation of the h is sufficient to get the average channel length statistics correct. However, at $t = 30$ and before the drainage divide is firmly established, the values of $\langle \sum L(\Omega) \rangle$ for $\Omega = 3$ are a sensitive measure, implying that the properties of third order basins are highly dependent on the structure of the main divide. While η^* is also high for $\Omega = 3$ for $t = 100$, the $\eta = 0$ case can attain the requisite values by chance. In contrast, in this case, it is the $\Omega = 1$ basins where additional structure is required to get the correct channel length statistics, with the surrogates producing lengths that are too short. The implication of the slopes being matched very well for small basins at $t = 100$ (Fig. 6c) but $\langle \sum L(\Omega = 1) \rangle$ being too small is that a simple multi-Hölder model cannot adequately represent either basin shape or valley sinuosity effects correctly.

4.3 Total number of basins

Three classical scalings for drainage basins as a function of stream order are the laws of stream number, stream length and basin area [*Rodgriguez-Iturbe and Rinaldo*, 1997]. Because we found that the behavior for basin area was similar to that for stream length, we do not report those results here, focusing instead on the stream number results, which in terms of our analysis we state as the number of basins of a given order, $N_B(\Omega)$ and present the results for $t = 100$ in Fig. 10. Here a much stronger effect was found in terms of significant differences at $\eta = 0$ for different stream orders less than $\Omega = 4$. Thus, $N_B(\Omega)$ is a more sensitive metric than $\langle \sum L(\Omega) \rangle$ for studying landscape complexity. In Fig. 11 we plot $\eta^*(N_B)$ for all four stream orders as a function of time. As with the results for dS/dA in Fig. 6b, a transition seems to emerge after about $t = 70$, but the effect is much more marked here: complexity measured by η^* really only increases once the flux

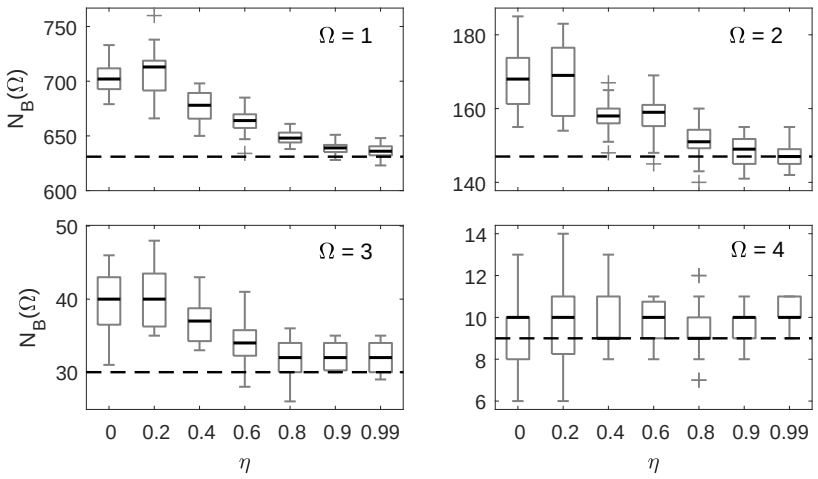

Figure 10. Boxplots showing the determination of $\eta^*(N_B)$ for the DEM at $t = 100$ for different basin orders, Ω. The values of N_B for the surrogates are shown as a function of η in each panel, with the dashed lines showing the value for the data itself. From these plots, $\eta^*(N_B) = \{0.9, 0.6, 0.6, 0.0\}$ for stream orders, 1 to 4, respectively. The boxplots are formulated in the same way as in Fig. 4.

steady-state is established for $t > 70$; it is only in the early stages of landscape that a simple multi-Hölder model is effective. Given that flux steady state was defined as the condition where the erosional fluxes balanced out the sediment provided by the rock uplift and was obtained by direct measurement during the experiment [*Singh et al.*, 2015], the congruence between the attainment of this state and the increase in η^* is rather remarkable. The implication is that complexity increases once diffusive forces gain greater prominence in the landscape dynamics.

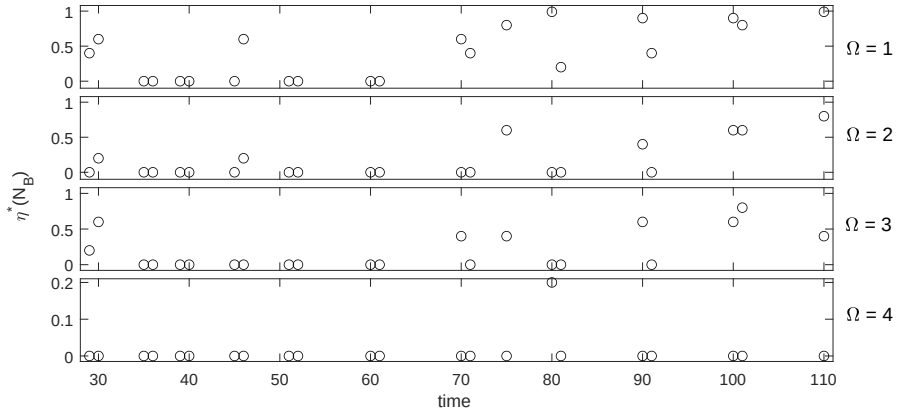

Figure 11. Values for $\eta^*(N_B)$ as a function of stream order, Ω (each panel) and time.

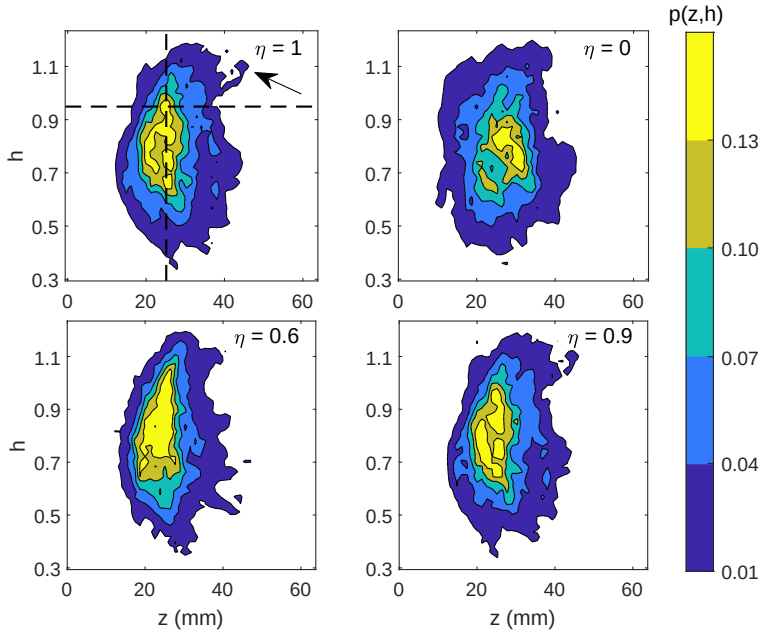

Figure 12. Probability contours for the joint distributions of the elevations, z, and Hölder exponents, h, for the DEM obtained at $t = 100$ for the original data (a) and three surrogate datasets at the value for η stated in each panel. Each surrogate DEM shown is that with the median RMSE between data and surrogates for the joint PDF. The dashed construction lines in panel (a) are the transects examined in Fig. 13 and the arrow identifies a feature discussed in the text.

5 The joint distribution of elevation and regularity

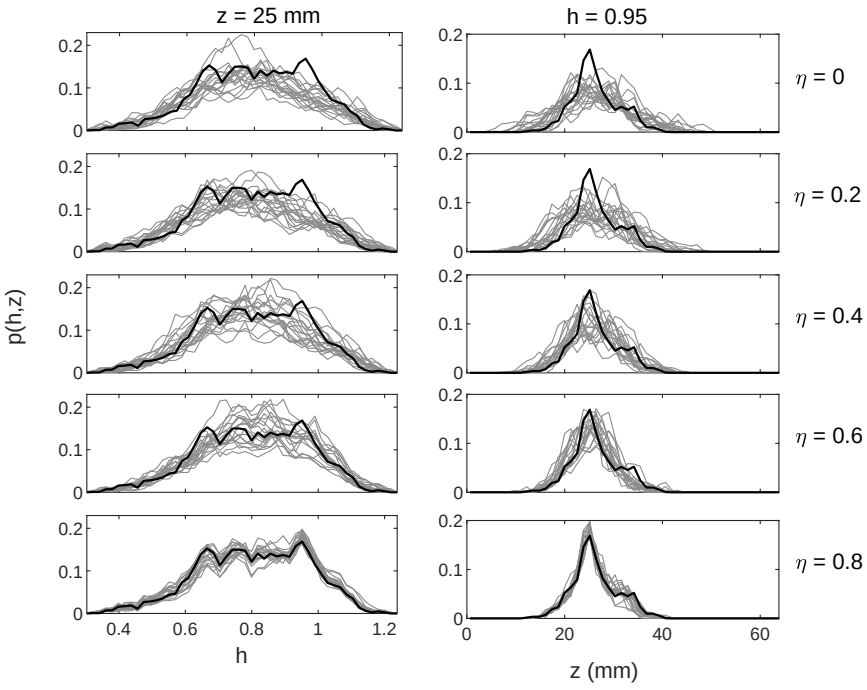

Figure 13. Transects through the joint PDF shown in Fig. 12a are shown in each panel as a solid line, together with the transects for nineteen surrogates at the stated value for η. The left-hand column of panels show the transect, $p(h|z = 25$ mm), i.e. the vertical line in Fig. 12a), while the right-hand column is for the horizontal line in Fig. 12a, i.e. $p(z|h = 0.95)$. The conditional distributions shown are not renormalized; they are transects through the joint PDF.

A recent extension to the classic hypsometry measure of *Strahler* [1952] examines the joint probability distribution function (PDF) between the elevations, z and the Hölder exponents, h [*Keylock et al.*, 2020b]. In other words, it captures the coupling that underpins the nature of a self-regulating landscape as defined in Table 1. The top-left panel of Fig. 12 shows this PDF for the original DEM at $t = 100$. The other panels show the results for the surrogate DEM with the median RMSE for different choices of η. Recall that our algorithm uses exactly the same z values. Hence, there is no difference in the marginal distribution for z and the hypsometries for all of these data are identical. However, there are clear differences in the shape of the joint PDFs and, as η increases, relatively subtle features of the original PDF, such as the outlying region identified by the arrow in the top-left panel, begin to be captured in the surrogates. Here we focus on two conditional distributions given by the transects through the joint distribution shown by the dashed lines in the upper left panel. These pass through the mode of the distribution at $z = 25$ mm, $h = 0.95$ and are given by the black line in each panel of Fig. 13. The gray lines in this figure are the equivalent conditional distributions for the surrogates at the stated value for η. It is clear that at low η, the surrogate data cannot replicate this mode, which is too large in magnitude for $p(z|h = 0.95)$ given in the right-hand column and is located at too high a value for h for $p(h|z = 25)$ in the left-hand column. A threshold value of $\eta^* = 0.4$ is appropriate from this analysis. Hence, once more, a simple multi-Hölder model cannot serve, and the key difficulty for such a model in terms of self-regulation is to have a sufficient number of intermediate elevations that are as smooth as $h = 0.95$.

Physically, this means that diffusive processes, which increase h at intermediate elevations, gain in geomorphic significance once the landscape attains a flux equilibrium, and are more important to the landscape structure than a simple multi-Hölder model can capture. This result is consistent with the earlier results that the simple multi-Hölder model produces too many basins of a given order (incision is excessive relative to diffusion) and has slopes that are over-steepened within the largest basins. Significant diffusive action on the intermediate slopes will result in fewer basins of intermediate order and will promote a reduction in average slopes for the larger watersheds of which these slopes are a part.

6 Application to two distinct topographies

While the experimental surfaces allow us to examine the evolution of a topography's response to a particular forcing, the idealized boundary conditions mean that there is not necessarily a relation to any specific observed terrain. As a consequence, in this section of the paper we examine the geomorphometry of two contrasting regions of the conterminous United States, Florida and Washington State, focusing on the slope-area scaling properties. The two DEMs were obtained from the USGS National Elevation Dataset at https://catalog.data.gov/dataset/usgs-national-elevation-dataset-ned and both cover an area of 20.48×20.48 km at a 1/3 arc-second (10 m) resolution. The particular drainage basins are the Ochlockonee River basin in Florida and the Cowlitz River basin in Washington State and these are shown in Fig. 14. The elevation range in the former is 0.5 m to 105 m, and is 263 m to 4100 m in the latter, while in the extracted regions, elevation ranges from 33.3 m to 100.8 m for the Florida case, and 361 m to 2274 m for the Washington case.

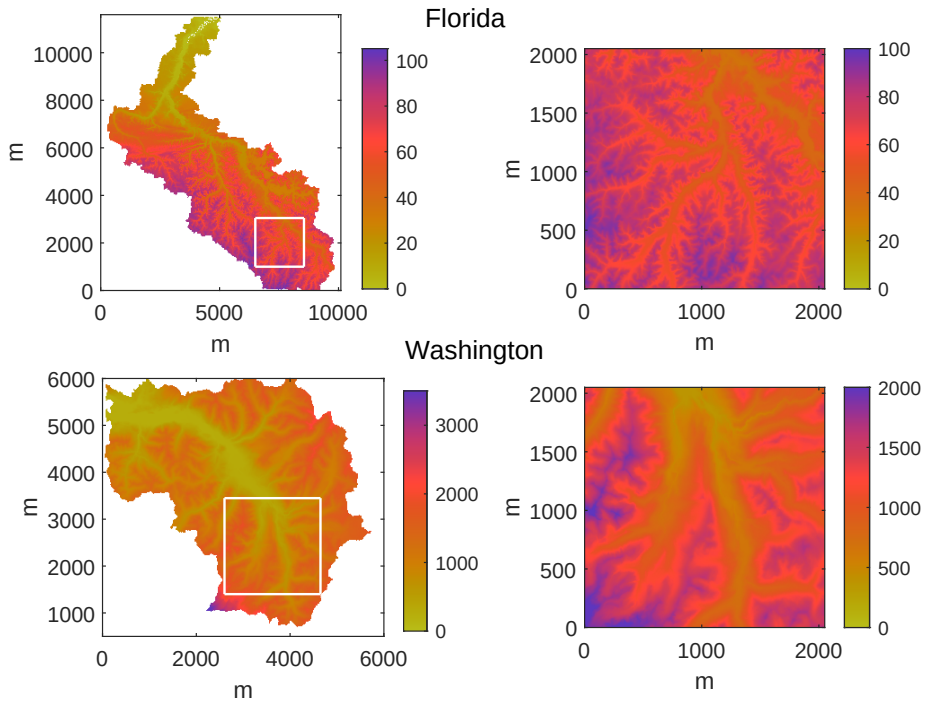

Figure 14. The two drainage basins from Florida (upper) and Washington State (lower) are shown in the left-hand panels, with the 2048 × 2048 m sub-regions that are analyzed in detail highlighted in the right-hand panels. The colorbars show the elevation range (m) in each panel.

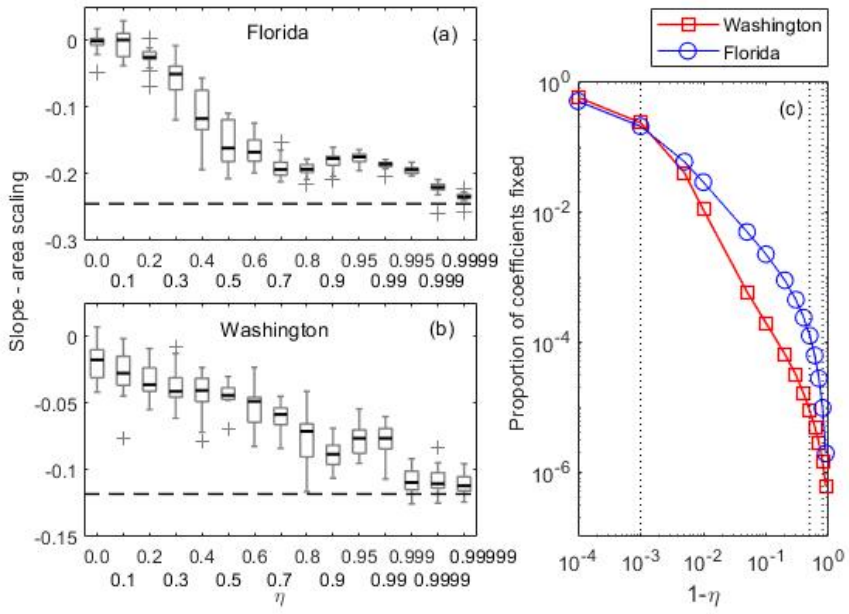

Figure 15. Values for the slope-area scaling exponent for the surrogate data as a function of η for Florida (a) and Washington (b), with the actual value shown as a horizontal, dashed line. Panel (c) shows the proportion of fixed wavelet coefficients as a function of $1 - \eta$ for the Washington and Florida DEMs. Vertical dotted lines highlight the values at, from left to right, $\eta = 0.999$, $\eta = 0.5$, $\eta = 0.2$ as discussed in the text.

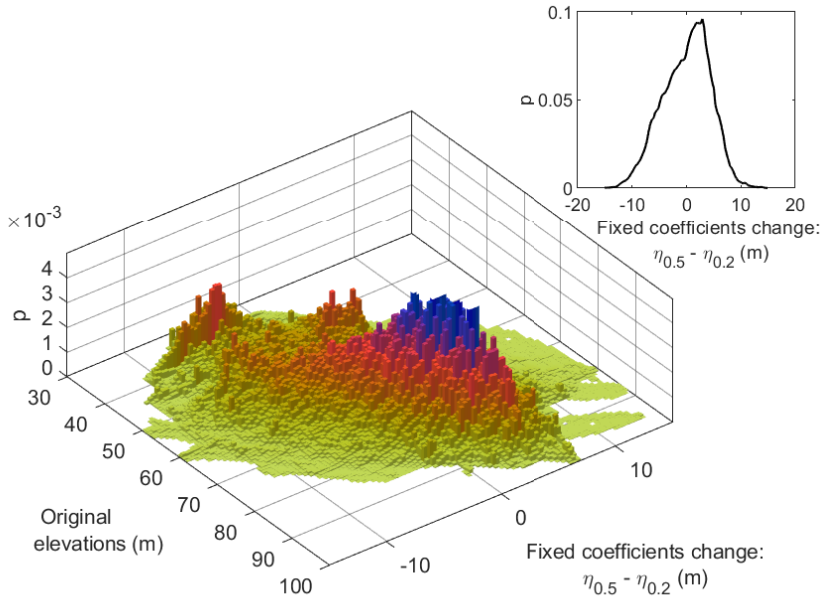

Figure 16. The joint probability distribution function of the difference in elevations between the DEMs reconstructed from the fixed wavelet coefficients at $\eta = 0.5$ and $\eta = 0.2$ versus the elevations in the original DEM. The marginal distribution for the former variable is shown in the inset panel.

Panels (a) and (b) in Fig. 15 show that the slope-area scaling for these two topographies is significantly different, with the scaling exponent nearly double in magnitude for the Florida case. Despite this difference, both basins have $\eta^* = 0.999$, although while the surrogates for the Washington DEM have a slope-area scaling exponent that converges on the true values in an approximately linear fashion, the Florida data exhibit a rapid decrease in the value of dS/dA for $0.2 < \eta \leq 0.5$ and a small increase for $0.8 < \eta \leq 0.95$. To investigate this further we examined the fixed wavelet coefficients at these choices for η. The proportion of fixed coefficients as a function of η is given in Fig. 15c. It is notable that for both DEMs, $\eta = 0.999$ equates to about 20% of the coefficients being fixed, but that for lower values for η (to the right in this panel) there is a clear divergence in the proportion of coefficients fixed between the two DEMs, with energy spread among a greater number of coefficients for the Florida case. We reconstructed the Florida DEM from the fixed coefficients at $\eta = 0.2$ and $\eta = 0.5$, and then found the difference between these DEMs. Thus, we examined how the topography fixed in place in the algorithm changed over this range of values for η. The inset in Fig. 16 shows the histogram of the elevation change between these two DEMs formed from the fixed coefficients. Clearly, the typical change is an increase by 5 m to the DEM elevations from $\eta = 0.2$ to $\eta = 0.5$. The main panel of Fig. 16 shows the joint PDF of the change in the elevations against the elevations in the original DEM. The modal change of +5m is concentrated between 60m and 80m although there are also two other modes: an incision mode where the elevation change is ~ -5m, concentrated in the lowest elevations ($\leq$ 40m), and another constructive mode where the elevation increases by $\sim$ 5m at low elevation (45 m). Consequently, we can conclude that the key difficulty for a multi-Hölder model in replicating the slope-area scaling for the Florida case-study is in allocating sufficient heights to these intermediate elevations. In other words, these regions in the terrain are dissected too much in the low η surrogates, while in nature the greater preponderance of diffusive processes preserves these elevations. This is consistent with the earlier analysis of the number of $\Omega = 1$ basins and of the slope-area scaling for the experimental surfaces. Preserving mass in the topography

in the 60m-80m elevation range at $\eta = 0.5$ results in greater slopes in the smaller area basins, changing the median slope-area scaling for the surrogates from -0.026 for $\eta = 0.2$ to -0.162 at $\eta = 0.5$.

7 Conclusion

In this paper we have formalized the nonlinear analysis of digital elevation models using the gradual multifractal reconstruction (GMR) framework. In particular, we have used experimental, evolving landscapes to show that a simple multi-Hölder model for terrain, even with the set of elevations, z, constrained to the original values and the pointwise Hölder exponents located correctly in the terrain, is not sufficient to replicate several measures of geomorphometry. Our analysis framework has shown that the slope-area scaling relation, dS/dA and, particularly, the number of basins for a given Horton-Strahler stream order (when this is less than the scale of the system studied) are sensitive measures of landscape structure. The slope-area scaling was also applied to regions of the same area from Florida and Washington State with an order of magnitude difference in elevation range. Despite very different values for dS/dA, the values for the GMR control parameter at which there was no significant difference between data and surrogates was very similar ($\eta^* = 0.999$) and very different to the value of $\eta^* = 0$ expected if a simple multi-Hölder or multifractal model is sufficient to describe the topography.

What was particularly notable in our experimental results was that once the landscape attained an equilibrium in terms of flux, the morphology was still evolving, and becoming more complex according to our significance testing framework. Indeed, it was only once this flux equilibrium was established that such an effect was clear. This was associated with the relative preponderance of diffusive phenomena such that, when a topography is in the early stages of evolving from a perturbation, a simple multi-Hölder stochastic process may be able to replicate most geomorphically relevant measures of landscape structure. However, when changes in flux become negligible, it is the subtle re-working of a landscape by more diffusive processes that results in an increase in landscape complexity as measured by η^*. This was particularly associated with the coupling between low or intermediate elevations and large Hölder exponents (smooth regions).

Our observations raise the question of which class of stochastic processes provides a potential guide to modeling mature landscape surfaces effectively. Our results in Figs. 12 and 13 are explicitly about the coupling between the Hölder exponents and the elevations themselves and that they demonstrate an association implies that self-regulating multi-Hölder surfaces [*Lévy Véhel*, 2013; *Echelard et al.*, 2015] may have some potential. It also lends support to the recent suggestion that hypsometric analysis can be usefully extended by simultaneous consideration of elevation and Hölder regularity [*Keylock et al.*, 2020b]. However, our results also reveal no simple relation between elevation and Hölder regularity, implying further conditioning is necessary as alluded to in Table 1. As noted in the introduction, *Veneziano and Iacobellis* [1999] proposed that differing Hölder regularity could be associated with the channel network and the hillslope and their hypothesis may have some potential based on our analysis. However, such an approach takes us full circle as the introduction began by contrasting geomorphic studies that focus on extracted landscape features with those that attempt to characterize the landscape as a whole, with the latter philosophy guiding the work presented here. Advances in digital terrain processing, [e.g. *Passalacqua et al.*, 2010], simplify the process of DEM classification and the next stage of our work is to form a set of landscape regimes and determine the Hölder conditioning for each, potentially also as a function of elevation. This will lead to a means to determine a statistical modeling framework for natural terrains. The hypothesis testing framework introduced here, or one similar in nature, will be needed to examine the functional relations between landscape regimes and Hölder regularity and, thus, the statistical significance of particular landscape regimes for such a model.

A: The IAAWT algorithm and gradual reconstruction

The IAAWT algorithm is based on a dual-tree complex wavelet transform (DTCWT) [*Kingsbury*, 2001; *Selesnick et al.*, 2005]. A pair of dyadic wavelet trees may be constructed to form a Hilbert pair [*Selesnick*, 2002], resulting in a complex transform. This can be achieved for orthogonal wavelets by offsetting the scaling filters by one half sample. The naïve approach would then be to deploy two trees of linear phase filters, of even length in one tree and odd in the other. However, such filters lack orthogonality and the sub-sampling structure is not particularly symmetric. Thus, *Kingsbury* [2001] formulated the *Q-shift* dual tree where, below the coarsest scale, all filters are even length, but no longer linear in phase. By designing the filters to have a delay of $\frac{1}{4}$ sample and by using the time reverse of one set of filters in the other tree, the required $\frac{1}{2}$ sample delay can be achieved. In this paper we use symmetric, biothorgonal filters with support widths of 13 and 19 values for the first level of the algorithm and *Q-shift* filters with a support of 14 values for all other levels on the dual tree (case C in *Kingsbury* [2001]). The *Q-shift* dual tree approach retains properties that make undecimated transforms advantageous for use in surrogate generation, such as shift invariance, but at a computational cost that is merely double that for a standard discrete wavelet transform. In addition, although we do not use it in this study, the transform also has enhanced directional selectivity compared to a classic discrete wavelet transform.

The IAAWT algorithm for a DEM containing elevations, $z(x, y)$, where $x = y = 2^J$, and where J is an integer, proceeds as follows:

1. Store the original elevations $z(x, y)$;
2. Apply the two-dimensional DTCWT and obtain wavelet amplitudes, $A_{k,\ell,j,p}$ and wavelet phases, $\omega_{k,\ell,j,p}$ over all $j = 1, \ldots, J$ scales for the $p = 1, \ldots, 6$ planes at each scale and for wavelet coefficient, w, with coordinates, (k, ℓ), where at each j there are $6 \times 2^{2(J-j)}$ coefficients:

$$\begin{aligned} A_{k,\ell,j,p} &= |w_{k,\ell,j,p}| \\ \omega_{k,\ell,j,p} &= \tan^{-1} \frac{\Im(w_{k,\ell,j,p})}{\Re(w_{k,\ell,j,p})}, \end{aligned} \tag{A.1}$$

   where $\Im$ is the imaginary part and $\Re$ is the real part of the wavelet coefficients, w;
3. Randomly sort the original elevations to give an initial elevation surface, $z^{(0)}$;
4. Take its two-dimensional DTCWT to derive randomised wavelet phases, $\omega^{(0)}_{k,j}$ for each scale and position;
5. Produce new $w^{(1)}_{k,j}$ by combining the original amplitudes with the randomised phases:

$$w^{(1)}_{k,j} = A_{k,j} \exp(i\omega^{(0)}_{k,j}) \tag{A.2}$$

6. Iterate the following steps until a convergence criterion is met, where at each step, s:
   (a) Take the inverse DTCWT to give a new DEM, $z^{(s)}(x, y)$ and then apply the amplitude adjustment step where a mapping is established between the original elevations, $z(x, y)$, and the $z^{(s)}(x, y)$ by rank-order matching to permit the values of $z^{(s)}$ to be replaced by the value in $z(x, y)$ with the same rank;
   (b) Take the DTCWT and obtain the new phases, $\omega^{(s)}_{k,j}$. Combine these with the original amplitudes, $A_{k,j}$ to give the $w^{(s+1)}_{j,k}$ using the s'th iterated variant of eq. (A.2).

Gradual multifractal reconstruction (GMR) generates synthetic data based on the IAAWT algorithm between limits of $\eta = 0$ (the original IAAWT algorithm) and $\eta = 1$ (the original dataset). Randomization is constrained between these limits to populate the

continuum with surrogate data. To do this we first define an energy measure that needs to account for the decimated nature of the dual tree complex transform by weighting the coefficients by a factor 2^j (i.e. we adopt an L1 norm):

$$E_\eta = \sum_{j=1}^{J} \sum_{p=1}^{6} \sum_{k=1}^{K} \sum_{\ell=1}^{L} \frac{|w_{k,\ell,j,p}|^2}{2^j} \tag{A.3}$$

That is, with $j = 1, \ldots, J$ scales, there are $K \times L$ coefficients, where $K, L = 2^{J-j}$ in each of six orientation planes at each scale, meaning that more energy will be associated with each coefficient on average at the larger j, necessitating the introduction of the denominator. We then place the absolute values for the $w_{k,\ell,j,p}$ in descending rank order and fix the first r coefficients such that $\frac{\sum_{r=1}^{K\times N} |w_r|^2}{E_\eta} \geq \eta$. This selected set of coefficients are fixed in place on the wavelet coefficient template, while the others are phase randomized using eq. (A.2).

Acronyms

DEM Digital elevation model
DTCWT Dual-tree complex wavelet transform
GMR Gradual multifractal reconstruction
GWR Gradual wavelet reconstruction
HECAS Hölder exponent-catchment area scaling
IAAFT Iterated amplitude-adjusted Fourier transform
IAAWT Iterated amplitude-adjusted wavelet transform
PDF Probability distribution function
RMSE Root-mean-squared-error
XLE Experimental Landscape Evolution

Acknowledgments

This work was supported by Royal Academy of Engineering/Leverhulme Trust Senior Research Fellowship LTSRF1516-12-89 awarded to the lead author, who was also supported by Loughborough University's HPC Hydra cluster. Digital elevations for the experimental data and the sub-regions of the Ochlockonee River basin and Cowlitz River basin used in this study may be obtained from http://doi.org/10.5281/zenodo.3922330.

References

Ali, N., A. Fuchs, I. Neunaber, J. Peinke, and R. B. Cal (2019), Multi-scale/fractal processes in the wake of a wind turbine array boundary layer, *Journal of Turbulence*, *20*(2), 93-120.

Arnéodo, A., E. Bacry, S. Jaffard, and J. F. Muzy, (1998), Singularity spectrum of multifractal functions involving oscillating singularities, *J. Fourier Analys. Appl.*, *4*, 159-174.

Arrell, K. E., P. F. Fisher, N. J. Tate, and L. Bastin, (2007), A fuzzy *c*-means classification of elevation derivatives to extract the morphometric classification of landforms in Snowdonia, Wales, *Comp. Geosci.*, *33*(10), 1366-1381.

Basu, S., E. Foufoula-Georgiou, B. Lashermes, and A. Arneodo (2007), Estimating intermittency exponent in neutrally stratified atmospheric surface layer flows: a robust framework based on magnitude cumulant and surrogate analyses, *Phys. Fluids*, *19*(11), 115102, doi:10.1063/1.2786001.

Benzi, R., L. Biferale, A. Crisanti, G. Paladin, M. Vergassola and A. Vulpiani (1993), A random process for the construction of multiaffine fields, *Physica D*, *65*, 352-358.

Boon III, J. D. and R. J. Byrne (1981), On basin hypsometry and the morphodynamic response of coastal inlet systems, *Marine Geol.*, *40*, 27-48.

Brocklehurst, S. H. and K. X. Whipple (2004), Hypsometry of glaciated landscapes, *Earth Surf. Proc. Land.*, *29*, 907-926, doi:10.1002/esp.1083.

Clubb, F. J., S. M. Mudd, D. T. Milodowski, M. D. Hurst, and L. J. Slater (2014), Objective extraction of channel heads from high-resolution topographic data, *Water Resour. Res.*, *50*, 4283-4304, doi:10.1002/2013WR015167.

Echelard, A., J. Lévy Véhel, and A. Philippe (2015), Statistical estimation for a class of self-regulating processes, *Scand. J. Stat.*, *42*(2), 485–503.

Ehsani, A. H. and F. Quiel (2008), Geomorphometric feature analysis using morphometric parameterization and artificial neural networks, *Geomorphology*, *99*(1-4), 1-12.

Evans, I. S. and C. J. McLean (1995), The land surface is not unifractal: variograms, cirque scale and allometry, *Zeit. für Geomorph. Suppl.*, *101*, 127-147.

Frisch, U. and G. Parisi (1985), The singularity structure of fully developed turbulence, in *Turbulence and Predictability in Geophysical Fluid Dynamics and Climate Dynamics* edited by M. Ghil, R. Benzi and G. Parisi, pp.84-88, Elsevier.

Gagnon, J.-S., S. Lovejoy, and D. Schertzer (2006), Multifractal earth topography, *Nonlin. Proc. Geophys.*, *13*(5), 541-570.

Gasparini, N.M., and K. X. Whipple (2014), Tectonic control of topography, rainfall patterns, and erosion during rapid post12 Ma uplift of the Bolivian Andes, *Lithosphere 6*(4) 251-268, doi:10.1130/L322.1.

Hack, J. T. (1957), Studies of longitudinal stream profiles in Virginia and Maryland, *U.S. Geol. Surv. Prof. Pap.*, *294-B*, 197.

Jaffard, S. (1997), Multifractal formalism for functions .1. Results valid for all functions, *SIAM J. Math. Anal.*, *28*, 944-970.

Jerolmack, D.J. and C. Paola (2010), Shredding of environmental signals by sediment transport, *Geophys. Res. Lett.37*(19), L19401.

Keylock, C. J. (2009), Evaluating the dimensionality and significance of active periods in turbulent environmental flows defined using Lipshitz/Hölder regularity, *Environ. Fluid Mech.*, *9*, 509-523.

Keylock, C. J. (2010), Characterizing the structure of nonlinear systems using gradual wavelet reconstruction, *Nonlinear Proc.Geophys.*, *17*, 615–632.

Keylock, C. J. (2012), A resampling method for generating synthetic hydrological time series with preservation of cross-correlative structure and higher order properties, *Water Resour. Res.*, *48*(W12521), doi:10.1029/2012WR011923.

Keylock, C. J. (2017), Multifractal surrogate-data generation algorithm that preserves pointwise Holder regularity structure, with initial applications to turbulence, *Phys. Rev. E*, *95*, 032,123.

Keylock, C. J. (2018), Gradual multifractal reconstruction of time-series: Formulation of the method and an application to the coupling between stock market indices and their Hölder exponents, *Physica D*, *368*, 1–9.

Keylock, C. J. (2019), Hypothesis testing for nonlinear phenomena in the geosciences using synthetic, surrogate data, *Earth Space Sci.*, *6*, doi: 10.1029/2018EA000435.

Keylock, C. J., M. Ghisalberti, G. G. Katul, and H. M. Nepf (2020a), A joint velocity–intermittency analysis reveals similarity in the vertical structure of atmospheric and hydrospheric canopy turbulence, *Env. Fluid Mech.*, *20*, 77-101, doi:10.1007/s10652-019-09694-w.

Keylock, C. J., K. Nishimura and J. Peinke (2012), A classification scheme for turbulence based on the velocity-intermittency structure with an application to near-wall flow and with implications for bedload transport, *J. Geophys. Res.*, *117*, F01037, doi: 10.1029/2011JF002127.

Keylock, C. J., A. Singh, and E. Foufoula-Georgiou (2014b), The complexity of gravel-bed river topography examined with gradual wavelet reconstruction, *J. Geophys. Res.*, *119*, 682–700, doi:10.1002/2013JF002999.

Keylock, C. J., A. Singh, P. Passalacqua and E. Foufoula-Georgiou (2020b), Hölder-conditioned hypsometry: A refinement to a classical approach for the characterization of topography, *Water Resour. Res*

Keylock, C. J., R. Stresing, and J. Peinke (2015) Gradual wavelet reconstruction of the velocity increments for turbulent wakes, *Phys. Fluids*, *27*, art. no. 025104.

Kingsbury, N. (2001), Complex wavelets for shift invariant analysis and filtering of signals, *Appl. Comput. Harmon. Anal.*, *10*, 234–253.

Klinkenberg, B., and M. F. Goodchild (1992), The fractal properties of topography: A comparison of methods, *Earth Surf. Proc. Land.*, *17*(3), 217-234.

Kolmogorov, A. N. (1941), The local structure of turbulence in incompressible viscous fluid for very large Reynolds numbers, *Dokl. Akad. Nauk. SSSR.*, *30*, 299-303.

Lague, D. and P. Davy (2003), Constraints on the long-term colluvial erosion law by analyzing slope-area relationships at various uplift rates in the Siwaliks Hills (Nepal), *J. Geophys. Res.*, *108*(2), ETG 8-1 - ETG 18-11.

Lavallée, D., S. Lovejoy, D. Schertzer, and P. Ladoy (1993), Nonlinear variability of landscape topography: multifractal analysis and simulation, in De Cola, L. and N. Lam, *Fractals in Geography*, p. 171-205, Prentice-Hall, Englewood, N.J.

Lévy Véhel, J. (2013), Beyond multifractional Brownian motion: New stochastic models for geophysical modelling, *Nonlin. Proc. Geophys.*, *20*(5), 643–655.

Lifton, N. A., and C. G. Chase (1992), Tectonic, climatic and lithologic influences on landscape fractal dimension and hypsometry: implications for landscape evolution in the San Gabriel Mountains, California, *Geomorphology*, *5*(1-2), 77-114.

Mandelbrot, B. and J. W. van Ness (1968), Fractional Brownian motions, fractional noises and applications, *SIAM Review*, *10*, 4, 422-437.

Outcalt, S.I. and M. A. Melton (1992), Geomorphic application of the HausdorffBesicovich dimension, *Earth Surface Processes and Landforms 17*(8), 775-787.

Passalacqua, P., T. Do Trung, E. Foufoula-Georgiou, G. Sapiro, and W. E. Dietrich (2010), A geometric framework for channel network extraction from lidar: Nonlinear diffusion and geodesic paths, *J. Geophys. Res*, *115* (1), F01002.

Peltier, R. F. and J. Lévy Véhel (1995), Multifractional Brownian motion: definition and preliminary results, *INRIA Tech. Report 2645*.

Perron, J. T., J. W. Kirchner, and W. E. Dietrich (2008), Spectral signatures of characteristic spatial scales and nonfractal structure in landscapes, *J. Geophys. Res.*, *113*(F04003), doi:10.1029/2007JF000866.

Poggi, D., A. Porporato, L. Ridolfi, J. D. Albertson, and G. G. Katul (2004), Interaction between large and small scales in the canopy sublayer, *Geophys. Res. Lett.*, *32*(L05102), 10.1029/2003GL018611.

Rodriguez-Iturbe, I., and A. Rinaldo (1997), *Fractal River Basins: Chance and Self-Organization*, Cambridge Univ. Press, New York.

Schreiber, T., and A. Schmitz (1996), Improved surrogate data for nonlinearity tests, *Phys. Rev. Lett.*, *77*, 635–638.

Schwenk, J., and E. Foufoula-Georgiou (2017), Are process nonlinearities encoded in meandering river planform morphology?, *J. Geophys. Res. Earth Surf.*, *122*, doi:10.1002/2016JF003,929.

Selesnick, I. (2002), The design of approximate Hilbert transform pairs of wavelet bases, *IEEE Trans. Sig. Proc.*, *50*, 1144–1152.

Selesnick, I., R. Baraniuk, and N. Kingsbury (2005), The dual-tree complex wavelet transform, *IEEE Signal Proc. Mag.*, *22*, 123.

Seuret, S. and J. Lévy Véhel (2003), A time domain characterization of 2-microlocal spaces, *J. Fourier Anal. Appl.*, *9*, 473-495.

Singh, A., L. Reinhardt, and E. Foufoula-Georgiou (2015), Landscape reorganization under changing climatic forcing: Results from an experimental landscape, *Water Resour. Res.*, *51*, 4320-4337, doi:10.1002/2015WR017161.

716 Strahler, A. N. (1952), Hypsometric (area-altitude) analysis of erosional topography, *Geol.*
717 *Soc. Am. Bull.*, *63*, 1117-1142.
718 Tejedor, A., A. Singh, I. Zaliapin, A. L.Densmore, and E. Foufoula-Georgiou (2017),
719 Scale-dependent erosional patterns in steady-state and transient-state landscapes, *Sci.*
720 *Adv.*, *3*, e1701683.
721 Theiler, J., S. Eubank, A. Longtin, B. Galdrikian, and J. Farmer (1992), Testing for non-
722 linearity in time series: the method of surrogate data, *Physica D*, *58*, 77–94.
723 Tokunaga, E. (1978), Consideration on the composition of drainage networks and their
724 evolution, *Tokyo Metro. Univ., Japan, Geograph. Rep.*, *13*, 1-27.
725 Venema, V., S. Meyer, S. G. Garcia, A. Kniffka, C. Simmer, S. Crewell et al. (2006), Sur-
726 rogate cloud fields generated with the iterative amplitude adapted Fourier transform al-
727 gorithm, *Tellus A*, *58*, 104-120.
728 Veneziano, D. and V. Iacobellis (1999), Self-similarity and multifractality of topographic
729 surfaces at basin and subbasin scales, *J. Geophys. Res. 104*(B6), 12797-12812.
730 Venugopal, V., S. Roux, E. Foufoula-Georgiou, and A. Arneodo (2006), Revisiting mul-
731 tifractality of high-resolution temporal rainfall using a wavelet-based formalism, *Water*
732 *Resour. Res. 42*(W06D14), doi:10.1029/2005WR004489.
733 Willgoose, G. (1994), A statistic for testing the elevation characteristics of landscape sim-
734 ulation models, *J. Geophys. Res.*, *99*(B7), 13987-13996, doi:10.1029/94JB00123.
735 Zanardo, S., I. Zaliapin, and E. Foufoula-Georgiou (2013), Are American rivers Tokunaga
736 self-similar? New results on fluvial network topology and its climatic dependence, *J.*
737 *Geophys. Res.: Earth Surf.*, *118*, 1-18, doi:10.1002/jgrf.20029.